ACS OMEGA

http://pubs.acs.org/journal/acsodf

Article

Concurrent Dual-Contrast Enhancement Using Fe_3O_4 Nanoparticles to Achieve a CEST Signal Controllability

Feixiang Hu, Dan Wang, Xiaowen Ma, Tingdan Hu, Yali Yue, Wei Tang, PuYe Wu, Tong Tong,* and Weijun Peng*

Cite This: *ACS Omega* 2023, 8, 24153−24164

Read Online

ACCESS | Metrics & More | Article Recommendations

ABSTRACT: Traditional T_2 magnetic resonance imaging (MRI) contrast agents have defects inherent to negative contrast agents, while chemical exchange saturation transfer (CEST) contrast agents can quantify substances at trace concentrations. After reaching a certain concentration, iron-based contrast agents can "shut down" CEST signals. The application range of T_2 contrast agents can be widened through a combination of CEST and T_2 contrast agents, which has promising application prospects. The purpose of this study is to develop a T_2 MRI negative contrast agent with a controllable size and to explore the feasibility of dual contrast enhancement by combining T_2 with CEST contrast agents. The study was carried out *in vitro* with HCT-116 human colon cancer cells. A GE SIGNA Pioneer 3.0 T medical MRI scanner was used to acquire CEST images with different saturation radio-frequency powers (1.25/2.5/3.75/5 μT) by 2D spin echo−echo planar imaging (SE-EPI). Magnetic resonance image compilation (MAGiC) was acquired by a multidynamic multiecho 2D fast spin−echo sequence. The feasibility of this dual-contrast enhancement method was assessed by scanning electron microscopy, transmission electron microscopy, Fourier transform infrared spectroscopy, dynamic light scattering, ζ potential analysis, inductively coupled plasma, X-ray photoelectron spectroscopy, X-ray powder diffraction, vibrating-sample magnetometry, MRI, and a Cell Counting Kit-8 assay. The association between the transverse relaxation rate r_2 and the pH of the iron-based contrast agents was analyzed by linear fitting, and the linear relationship between the CEST effect in different B_1 fields and pH was analyzed by the ratio method. Fe_3O_4 nanoparticles (NPs) with a mean particle size of 82.6 ± 22.4 nm were prepared by a classical process, and their surface was successfully modified with −OH active functional groups. They exhibited self-aggregation in an acidic environment. The CEST effect was enhanced as the B_1 field increased, and an *in vitro* pH map was successfully plotted using the ratio method. Fe_3O_4 NPs could stably serve as reference agents at different pH values. At a concentration of 30 μg/mL, Fe_3O_4 NPs "shut down" the CEST signals, but when the concentration of Fe_3O_4 NPs was less than 10 μg/mL, the two contrast agents coexisted. The prepared Fe_3O_4 NPs had almost no toxicity, and when their concentration rose to 200 μg/mL at pH 6.5 or 7.4, they did not reach the half-maximum inhibitory concentration (IC_{50}). Fe_3O_4 magnetic NPs with a controllable size and no toxicity were successfully synthesized. By combining Fe_3O_4 NPs with a CEST contrast agent, the two contrast agents could be imaged simultaneously; at higher concentrations, the iron-based contrast agent "shut down" the CEST signal. An *in vitro* pH map was successfully plotted by the ratio method. CEST signal inhibition can be used to realize the pH mapping of solid tumors and the identification of tumor active components, thus providing a new imaging method for tumor efficacy evaluation.

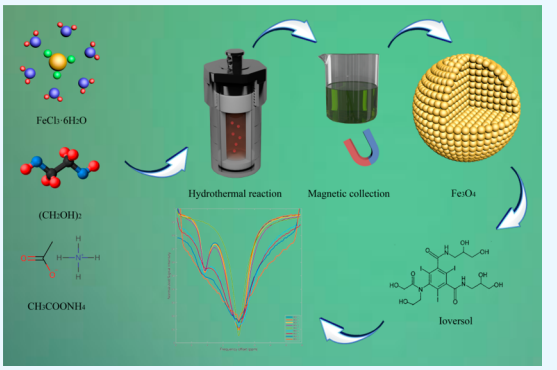

INTRODUCTION

Traditional imaging is used primarily to observe the final, cumulative effect of molecular changes in lesioned cells: i.e., visible anatomical or morphological changes. In contrast, molecular imaging can be used to detect anomalies at the cellular and molecular levels in early lesions before the emergence of diseases with anatomical or morphological changes. The microenvironment of tumors differs from that of normal tissues; thus, the early detection of microenvironmental changes can greatly improve the early diagnosis of tumors.[1] Fe_3O_4 nanoparticles (NPs) are traditional magnetic NPs that are widely used in the biomedical field due to their excellent magnetic properties, good biocompatibility, low cytotoxicity, and biodegradability.[2−5]

Fe_3O_4 NPs are usually used as a classic T_2 contrast agent in magnetic resonance imaging (MRI), but when the diameter of the Fe_3O_4 NP is less than 5 nm, the decrease in magnetic moment will strongly inhibit the T_2 effect or enhance the T_1 effect. Thus, adjusting the size of Fe_3O_4 NPs can produce a switchable MR contrast agent in response to T_1/T_2 signals.[2,6] Fe_3O_4 NPs also have an excellent thermal effect in an oscillating magnetic field and thus have been widely used in magnetic thermotherapy for tumors.[3] Fe_3O_4 NPs have catalytic activity similar to that of peroxidase and can catalyze the conversion of

Received: October 31, 2022
Accepted: February 13, 2023
Published: June 29, 2023

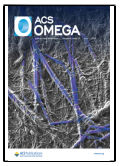

endogenous hydrogen peroxide into highly cytotoxic hydroxyl radicals (•OH) through the Fenton reaction, resulting in tumor cell death.[7,8] Such chemodynamic therapy based on the Fenton reaction has been an emerging direction in cancer treatment in recent years, bringing new applications of Fe_3O_4 NPs.[9] In this paper, Fe_3O_4 NPs, highly representative magnetic NPs with many advantages, were used to explore the impact of changes in the acidity of the tumor microenvironment and were combined with chemical-exchange saturation transfer (CEST) contrast agents to investigate the feasibility of dual-contrast enhancement.

Metabolic changes are the core marker of tumors. Characterizing the tumor microenvironment by monitoring changes in metabolites *in vivo* is a popular research topic but still faces difficulties, and noninvasive imaging is fundamental to clarify all aspects of tumor biology. The current research dilemma is that the concentration of tumor metabolites is low, and detection and quantitative analysis are difficult. CEST is an imaging technique based on the principle of chemical exchange and magnetization transfer between exchangeable protons and H_2O molecules. CEST can detect a substance's concentration on the millimolar or even micromolar scale, thus greatly increasing the imaging sensitivity. Tumor metabolites can be noninvasively detected by CEST imaging.[10] The use of ferrite to inhibit the CEST signal can reflect the distribution of active components in the tumor, which is conducive to defining tumor components and fibrosis after treatment. Only specific endogenous metabolites of the tumor, such as creatine or lactic acid metabolites, can produce CEST signals. If there is no metabolite aggregation in areas of tumor necrosis or cystic fibrosis, CEST signals cannot be generated, which is conducive to future applications and tumor efficacy evaluation. Now, with the clinical application of PET-MRI, our research can not only achieve iodine contrast imaging in X-rays but also achieve CEST and T_2 negative contrast MRI. This research is the first step to achieving clinical application.

In this experiment, ioversol, a CEST exogenous contrast agent, was used for imaging. Ioversol molecules have two amide groups, which generate a CEST peak at 4.3 ppm. CEST effects of different intensities are generated upon excitation on different radio-frequency (RF) B_1 fields. Therefore, changes in pH in the microenvironment can be calculated by the ratio method, thus avoiding interference from the contrast agent concentration.[11] It is often difficult to visualize disease pathology by multimodal imaging due to the superposition of various functional components.[12] The major advantage of CEST contrast agents is that their enhancement mode can be controlled; that is, the contrast is detectable only when the saturation pulse is applied to the specific resonance frequency of the contrast agent's exchangeable protons. Such switchability enhances the likelihood that CEST contrast agents will coexist with T_1/T_2 contrast agents. Superparamagnetic iron oxide (SPIO) NPs and CEST contrast agents, when used to label different cell populations, are capable of simultaneous imaging and tracking of two different cell populations, and SPIO can suppress the CEST signal. When the NP concentration increases, the CEST signal decreases. In other words, the CEST signal intensity decreases at the sites of concentration of Fe_3O_4 NPs in viable tissues.[13] Based on the above theory, Fe_3O_4 NPs and ioversol were combined for imaging for the first time in this paper. The interaction mechanism between the two contrast agents was explored in a pilot study, and *in vitro* MRI was conducted using the two contrast agents to assess the feasibility of using Fe_3O_4 NPs at different concentrations to inhibit the CEST signal. The results showed that these two contrast agents could be used simultaneously at a distinguishable range of concentrations.

MATERIALS AND METHODS

Materials. Ferric chloride hexahydrate ($FeCl_3{\cdot}6H_2O$, AR-99, 500 g), ethylene glycol ($(CH_2OH)_2$, 99, 500 mL), and ammonium acetate (CH_3COONH_4, AR-98, 500 g) were purchased from Rhawn Reagent (Shanghai, China). Citric acid ($C_6H_8O_7$, AR-99.5, 500 g), sodium citrate ($C_6H_5Na_3O_7$, 98, 500 g), and agar powder ($(C_{12}H_{18}O_9)$n, BR, 250 g) were purchased from MACKLIN Reagent (China). Phosphate-buffered saline (PBS, 500 mL) and sterile deionized water (H_2O) were obtained from Shanghai BasalMedia Technologies Co., Ltd. Ethanol (CH_3CH_2OH, analytically pure) and ioversol ($C_{18}H_{24}I_3N_3O_9$, 320 mg I/mL) were obtainedfrom Sinopharm Chemical Reagent Co., Ltd. and Jiangsu Hengrui Pharmaceuticals Co., Ltd., respectively.

Preparation of Fe_3O_4 NPs under Different Conditions. In a pilot study, the preparation of NPs was optimized. Fe_3O_4 NPs of different sizes were successfully prepared, and their particle size and morphological features were preliminarily determined by transmission electron microscopy (TEM). To synthesize SPIO nanoparticles (SPIONs) by a hydrothermal process, the precursors and surfactants were first dissolved in an alcohol−water solution through ion complexation and then transferred to a high-pressure stainless steel reactor lined with polytetrafluoroethylene, followed by a sealing reaction. Magnetic NPs of a specific particle size and morphology, such as Fe_3O_4 nanoflowers,[14] can be synthesized under high temperature and high pressure, and different particle sizes, morphologies, and magnetic properties can be obtained by altering the reaction parameters, such as heating temperature, reaction duration, and proportions of precursors and surfactants.[15] In this paper, the solution was heated at 200 °C for 4, 8, 12, and 16 h. At 8 h, the reaction volume was reduced by half, that is, the pressure inside the reactor was reduced, and the differences in reaction products at 160 and 200 °C were observed for 16 h. Finally, based on the particle size and morphology observed by TEM combined with the reaction time effect and product characteristics, a high-pressure reaction at 200 °C for 12 h was selected as the reaction conditions for the experiments.

Preparation of Fe_3O_4 NPs. First, magnetic Fe_3O_4 NPs were synthesized. All chemical reagents used in this experiment were of analytical grade and were used directly without further purification. Spherical magnetic Fe_3O_4 NPs were prepared by the hydrothermal method: 1.350 g of $FeCl_3{\cdot}6H_2O$ was dissolved in 70 mL of $(CH_2OH)_2$, followed by ultrasonic oscillation and magnetic stirring at room temperature until the material dissolved completely and the solution became orange-yellow and transparent. Then, 3.854 g of CH_3COONH_4 was added to the solution, followed by further ultrasonic oscillation and magnetic stirring at room temperature for ∼30 min until the material dissolved completely and the solution became yellow-brown and milky. Later, the solution was transferred to a 100 mL stainless-steel hydrothermal reactor lined with polytetrafluoroethylene and placed in an air-drying oven at 200 °C for a 12 h hydrothermal reaction. After the autoclave cooled naturally to room temperature, black magnetic precipitates were collected using a permanent magnet and washed with absolute ethanol and deionized water four times each. Finally, the NPs were thoroughly washed and dried in a drying oven at 80 °C overnight, and the resulting black powdery substance was used.

https://doi.org/10.1021/acsomega.2c07000
ACS Omega 2023, 8, 24153−24164

Characterization of Nanoparticles. The morphology and particle size of the NPs were observed by field-emission TEM (JEM 2100F, JEOL, Japan) and field-emission scanning electron microscopy (SEM) (SU8020, Hitachi, Japan). The active functional groups modified on the surface of the particles were analyzed using a Fourier transform infrared (FT-IR) spectrometer (Nicolet IS10, Nicolet, USA). The hydrodynamic size and the surface potential were measured by dynamic light scattering (Zetasizer Nano ZS90, Thermo Fisher, USA) and ζ potential analysis, respectively. The concentration of Fe^{3+} was measured via inductively coupled plasma atomic emission spectrometry (ICP-AES) (Agilent ICPOES730, Agilent, USA). The ionic valency and crystal morphology of the NPs were separately analyzed through X-ray photoelectron spectroscopy (XPS) (Thermo ESCALAB 250Xi, Thermo Fisher, USA) and X-ray powder diffraction (XRPD) (Bruker D8 ADVANCE, Bruker, Germany). A vibrating-sample magnetometer (VSM) (SQUID-VSM MPMS-3, Quantum Design, USA) was employed to measure the saturation magnetization value (M_s). Moreover, the characteristics of the element distribution were analyzed by energy-dispersive spectroscopy (EDS), and MRI (SIGNA Pioneer 3.0-T, GE, USA) was adopted for image acquisition and signal analysis of different MRI sequences.

***In Vitro* MRI Parameter Settings.** A GE SIGNA Pioneer 3.0 T Medical MRI scanner was used for *in vitro* MRI, and an eight-channel head coil was used for RF excitation and signal reception. T_1-weighted imaging (T_1WI) was acquired by a 2D fast spin−echo (FSE) sequence (field of view (FOV) 220 × 176 mm, matrix 224 × 192, slice thickness/gap 3/0.5 mm, number of slices 8, repetition time (TR) 400 ms, echo time (TE) 8 ms, echo train length (ETL) 3, bandwidth 31.25 kHz, number of excitations (NEX) 2). T_2-weighted imaging (T_2WI) was acquired by a 2D FSE sequence (FOV 220 × 176 mm, matrix 224 × 192, slice thickness/gap 3/0.5 mm, number of slices 8, TR 2575 ms, TE 120 ms, ETL 10, bandwidth 31.25 kHz, NEX 2). CEST images with different saturation RF powers (1.25/2.5/3.75/5 μT) were acquired by a 2D spin−echo echo-planar imaging sequence (FOV 220 × 176 mm, matrix 96 × 64, slice thickness 6 mm, number of slices 1, TR 4000 ms, TE 25 ms, bandwidth 250 kHz, NEX 1, off-resonance frequency 1000:25:1000 Hz). Magnetic resonance image compilation (MAGiC) was acquired by a multidynamic multiecho 2D FSE sequence (FOV 220 × 176 mm, matrix 224 × 192, slice thickness/gap 3/0.5 mm, number of slices 20, TR 4000 ms, TI 210/610/1810/3810 ms, TE 14.3/85.8 ms, ETL 12, bandwidth 31.25 kHz, NEX 1).

***In Vitro* MRI of Fe_3O_4.** *In vitro* GE MAGiC sequence (including T_1 and T_2 mapping sequences) scanning was performed using Fe_3O_4 nanomolecular probes. First, an appropriate amount of Fe_3O_4 NP powder was weighed, placed in a 10 mL centrifuge tube after the Fe^{3+} concentration was quantified by ICP, and diluted with PBS at different pH values until the volume of solution in each tube was 8 mL. Then, the solution was added to a small amount of agar powder (2%), dissolved by heating to 90 °C, and ultrasonically dispersed, followed by cooling to solidification for later testing. After that, the centrifuge tubes were arranged horizontally from left to right according to the concentration gradient of Fe^{3+} (0.015625, 0.03125, 0.0625, 0.125, 0.25, and 0.5 mM) and vertically from bottom to top according to pH (5.0, 6.7, and 7.4) and placed in homemade kits surrounded by pure water (Figure 1). Finally, the kits were subjected to routine T_1WI, T_2WI, and MAGiC sequence scanning in the head coil of the GE SIGNA Pioneer 3.0 T Medical MRI scanner, and the raw data were sent to a postprocessing workstation through the Picture Archiving and Communication Systems (PACS) to measure the T_1 and T_2 values.

CEST Effect of Ioversol under Different Conditions. CEST imaging was performed on the contrast agent ioversol to observe the changes in the CEST effect of ioversol at different pH values and field strengths. Ioversol solutions (42 mM) at different pH values (6.4, 6.6, 6.8, 7.0, 7.2, 7.4, and 7.6) were prepared and scanned in different B_1 fields (1.25, 2.5, 3.75, and 5.0 μT) to obtain their CEST Z-spectra. Ioversol has two amide groups that give rise to a CEST peak at 4.3 ppm. Finally, the kits were subjected to CEST sequence (±4.3 ppm) scanning in the head coil of the GE SIGNA Pioneer 3.0 T Medical MRI scanner. The raw data were sent to a postprocessing workstation through PACS, followed by linear fitting of the CEST effect and pH. In addition, the Z-spectra at different pH values and under different B_1 fields were plotted.

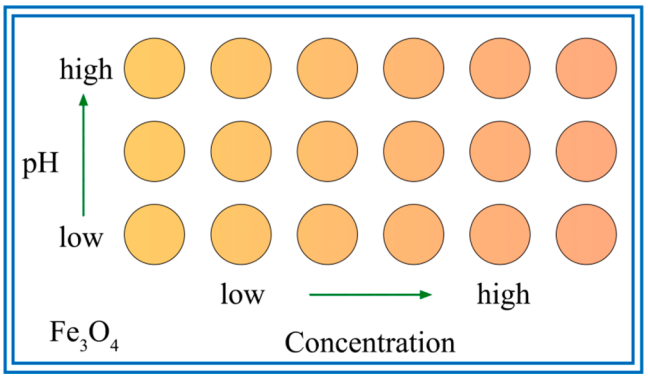

Figure 1. Schematic diagram of the positional arrangement of the Fe_3O_4 NP samples in magnetic resonance scanning according to pH value (5.0, 6.7, and 7.4) and Fe concentration (0.015625, 0.03125, 0.0625, 0.125, 0.25, and 0.5 mM).

Inhibition of the CEST Effect by Different Concentrations of Fe_3O_4. Fe_3O_4 at different Fe^{3+} concentrations (0, 0.005, 0.05, 0.5, 5, 10, 20, and 30 μg/mL) was added to ioversol (420 mM) solution using PBS (pH 7.4) as the solvent. Fe_3O_4 (0.5 μg/mL) control groups without ioversol were also prepared. Next, 18 mL of the solution was transferred to a 20 mL glass bottle, and a small amount of agar powder (2%) was added, dissolved by heating, mechanically stirred, and dispersed, followed by cooling to solidification for later testing. The glass bottles in the study groups were then arranged in order by Fe^{3+} concentration (0, 0.005, 0.05, 0.5, 5, 10, 20, and 30 μg/mL), while those in the control groups were placed next to the study group samples. All samples were placed in homemade kits surrounded by pure water. Finally, the kits were subjected to T_1WI, T_2WI, MAGiC, and CEST sequence scanning in a 1.25 μT B_1 field in the head coil of the GE SIGNA Pioneer 3.0 T Medical MRI scanner. The raw data were sent to an AW4.6 postprocessing workstation through PACS to measure the T_1, T_2, and amide proton transfer (APT) values. Moreover, the Z-spectra and magnetization transfer ratio asymmetry (MTR_{asym}) images were plotted.

Detection of the *In Vitro* Cytotoxicity of the NPs by the CCK-8 Assay. HCT-116 human colon cancer cells were resuscitated and cultured under specific conditions, and they were adjusted to the best state for later experiments. Next, the cells were plated. Specifically, the cultured HCT-116 cells (in

https://doi.org/10.1021/acsomega.2c07000
ACS Omega 2023, 8, 24153−24164

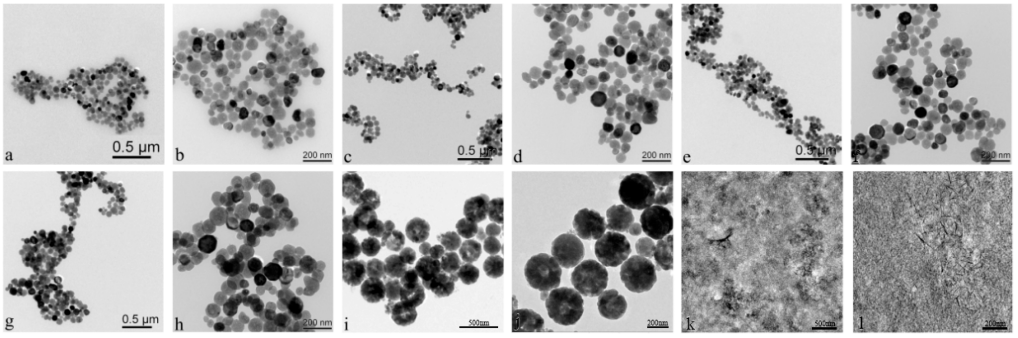

Figure 2. (a,b, e,f, g,h, and i,j) TEM images (500 and 200 nm, respectively) of reaction products at 4, 8, 12, and 16 h of reaction, respectively, at constant temperature (200 °C) and pressure. When the temperature was held at 200 °C, the reaction volume was reduced by half, while the reaction capacity remained unchanged; that is, the reaction pressure was reduced. (c,d) TEM images (500 and 200 nm, respectively) of reaction products after 8 h of heating. (k,l) TEM images (500 and 200 nm, respectively) of reaction products after 16 h of heating at a reaction temperature of 160 °C and constant pressure.

logarithmic growth phase, 80−90% confluence) in one bottle were washed with an appropriate amount of PBS and digested with an appropriate amount of trypsin in an incubator at 5% CO_2 and 37 °C for 1−2 min. After confirming under a microscope that all cells were digested, the digestion was terminated with 10% fetal bovine serum (FBS) containing Dulbecco's modified Eagle medium (DMEM), and the cells were pipetted evenly and centrifuged in a 50 mL centrifuge tube at 1000 rpm for 5 min. After discarding the supernatant, the cells were resuspended in 10% FBS-containing DMEM. Then, 20 μL of cells was mixed evenly with 20 μL of trypan blue, counted with a cell counter, and diluted with 10% FBS-containing DMEM until the cell density reached 3×10^4 cells/mL. One hundred microliters of mixed cells was added to each well of a 96-well plate (3000 cells/well) using a pipet, followed by the addition of 100 μL of DMEM, and the plate was incubated at 5% CO_2 and 37 °C overnight. Finally, the half-maximum inhibitory concentration (IC_{50}) was determined. (1) Samples were diluted with medium in a gradient up to 5-fold, with a total of eight concentrations including the stock solution (0.00256, 0.0128, 0.064, 0.32, 1.6, 8, 40, and 200 μg/mL). (2) The culture supernatant was aspirated from the 96-well plate using a pipet, and 100 μL of the test agent was added, with three parallel wells for each gradient. In addition, negative controls (with 100 μL of medium added) and blank controls (with 100 μL of medium added, without cells) were prepared and cultured in a 5% CO_2 incubator at 37 °C. The IC_{50} was detected at 24, 48, and 72 h. (3) Color development and reading were carried out as follows. First, the developing solution was prepared (DMEM:CCK-8 solution = 10:1) and mixed evenly. After the supernatant in each well was discarded using a pipet, 110 μL of developing solution was added to each well, taking care to avoid bubbles in the wells, which would affect the optical density (OD) reading. The plate was cultured in the incubator for approximately 0.5 h. Next, the 96-well plate was placed in the slot in a normal direction after the microplate reader was preheated for 10 min, followed by measurement and reading of the OD at 450 nm, and the data were exported to Excel. (4) For data processing and analysis, the average of the three OD values at 450 nm was taken for each sample. Next, with the concentration of the test agent as the abscissa and the cell survival rate as the ordinate, logarithmic curve fitting was performed in Excel to calculate the IC_{50} of the test agent against tumor cells.

Data Statistics and Analysis. The r_2 values under different pH conditions were obtained by linear fitting. A linear fitting method was also used to evaluate the relationship between the CEST effect and pH. In CEST analysis, one of the most important parameters is the magnetic transfer ratio asymmetry (MTR_{asym}), sometimes called CEST asymmetry, which is expressed by the formula

$$MTR_{asym}(\Delta\omega) = \frac{S(-\Delta\omega) - S(\Delta\omega)}{S_0}$$

where $\Delta\omega$ is the frequency offset, $S(-\Delta\omega)$ and $S(\Delta\omega)$ are the signal intensities on the positive and negative sides of the CEST spectrum or the Z spectrum, respectively, and S_0 is the unsaturated signal intensity. MTR_{asym} measurement analysis provides information about the CEST contrast enhancement scale resulting from the CEST signal calculated by the asymmetric analysis.

The cell survival rate was calculated as $[(A_s - A_b]/(A_c - A_b)] \times 100\%$, where A_s, A_c, and A_b are the average values of the study replicates (medium containing cells, CCK-8 solution, and test agent), control replicates (medium containing cells, CCK-8 solution, and no test agent), and blank replicates (medium without cells or test agent and containing CCK-8 solution), respectively. The x value where the cell survival rate was 50% ($y = 0.5$) was the IC_{50} value.

RESULTS

Synthesis of Fe_3O_4 Magnetic NPs. In this study, highly pure Fe_3O_4 NPs of the appropriate size were prepared under different experimental conditions. First, the reaction temperature was set to a constant 200 °C, the pressure was unchanged, and the particle size was controlled by changing the heating time, as shown in Figure 2 (Figure 2a,b, reaction time of 4 h; Figure 2e,f, reaction time of 8 h; Figure 2g,h, reaction time of 12 h; Figure 2i,j, reaction time of 16 h). TEM images showed that the NPs became larger with heating time (4−16 h) under constant temperature and pressure. At 16 h, magnetic microspheres of approximately 200 nm were obtained. With the extension of the reaction time, the Fe_3O_4 particles continued to crystallize and fuse, thus increasing the particle size. Compared with Figure 2e,f, the particle size changed little (Figure 2c,d) when the temperature was maintained at 200 °C, the reaction volume was reduced by half, the reaction capacity remained unchanged, that is, the reaction pressure was reduced, and the heating time was 8 h. The reason that the particle size did not change is that the total volume of the reactor was only 100 mL, and reducing the volume by half was not adequate to affect the (sealed) high-

https://doi.org/10.1021/acsomega.2c07000
ACS Omega 2023, 8, 24153−24164

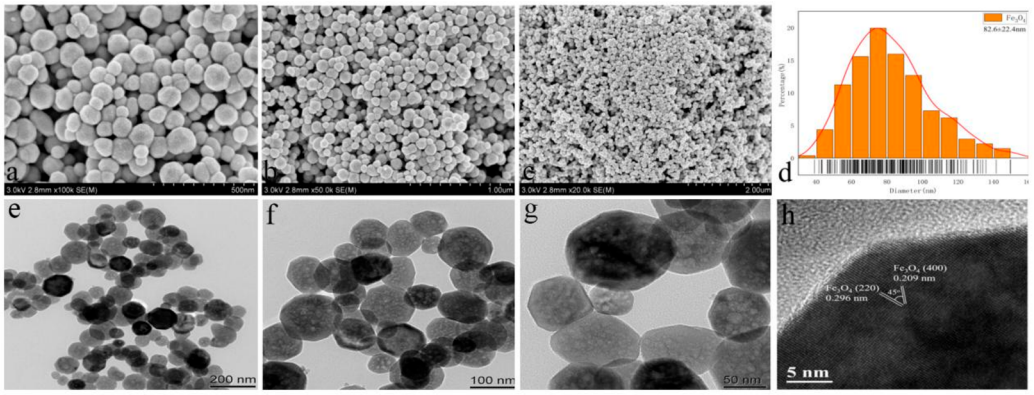

Figure 3. (a−c) Morphology of Fe_3O_4 NPs at different resolutions (500, 1000, and 2000 nm, respectively). (d) Statistical results of the average particle size of Fe_3O_4 NPs. TEM images of Fe_3O_4 magnetic NPs at different resolutions: (e) 200 nm, (f) 100 nm, (g) 50 nm, and (h) 5 nm.

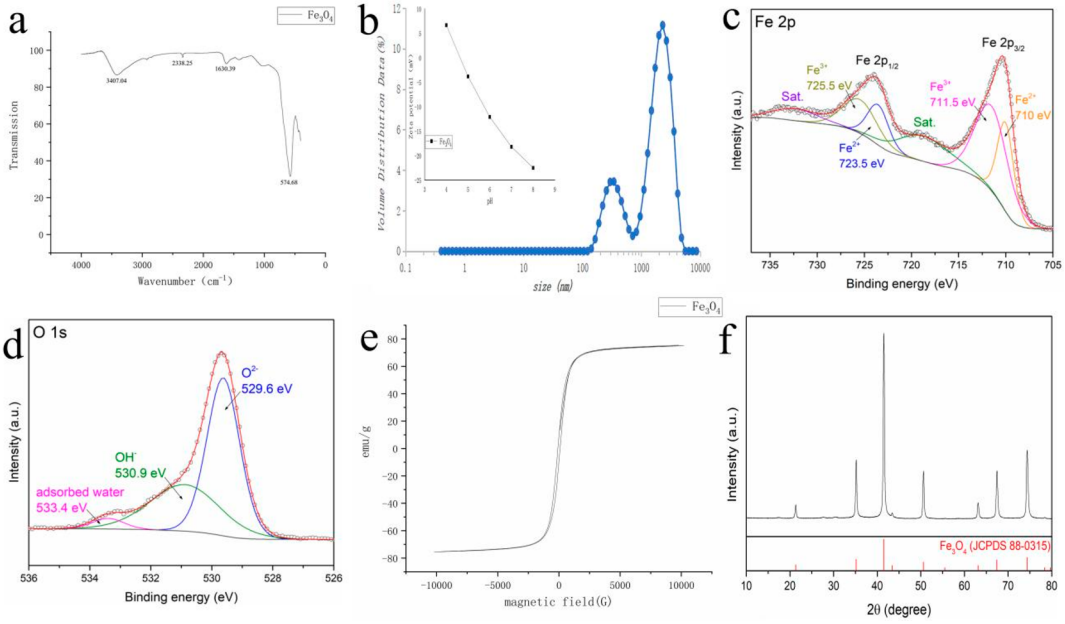

Figure 4. (a) Infrared spectrum of Fe_3O_4 NPs for imaging and (b) Fe_3O_4 hydrodynamic size distribution and ζ potential at different pH values. XPS fine spectra of (c)Fe and (d) O in Fe_3O_4 magnetic NPs. (e) The Fe_3O_4 M_s value is 75.45 emu/g. (f) XRD spectrum of Fe_3O_4 magnetic NPs.

pressure environment. In addition, under the same pressure, when the reaction temperature was reduced to 160 °C for 16 h, no NPs were formed, but less-developed hydroxide was obtained (Figure 2k,l), suggesting that a lower reaction temperature is not conducive to the crystallization of NPs.

Characterization of Fe_3O_4 Magnetic NPs. *SEM Results.* When we looked at the morphology at different resolutions by SEM (Figure 3a−c), the Fe_3O_4 NPs were spherical and smooth on the surface. As shown in Figure 3d, the mean particle size of the Fe_3O_4 NPs was 82.6 ± 22.4 nm, and the particle size was normally distributed. The particle size distribution of synthesized Fe_3O_4 was uniform and concentrated under our experimental conditions.

TEM Results. The morphology of Fe_3O_4 magnetic NPs was observed by TEM. As shown in Figure 3e−g (200, 100, and 50 nm, respectively), most of the NPs were spheroidal, and some were octahedral. There were many small pores in the magnetic NPs and even hollow structures in some, which were attributed to the process of aggregation and recrystallization. In other words, the tiny crystals that were initially generated formed loose microspheres, and new crystals were continuously generated and became attached to the surface of the microspheres. As the reaction continued, small crystals inside were prone to dissolution and recrystallization due to high surface energy and solubility and crystallized on the outer surface of the microspheres, thus gradually leading to small pores and even hollow structures in the microspheres.

A high-resolution TEM image (5 nm) of the Fe_3O_4 NPs is shown in Figure 3h. Clear lattice fringes with two different spacings (0.296 and 0.209 nm) were visible, corresponding to the (220) and (400) crystal planes of Fe_3O_4 (JCPDS 88-0315, cubic phase, $a = b = c = 8.375$ Å, $\alpha = \beta = \gamma = 90°$).[16] Moreover, the measured angle between the (220) and (400) crystal planes in the figure was 45°, the same as its theoretical value.

FT-IR Spectra. According to the FT-IR spectra of the Fe_3O_4 magnetic NPs (Figure 4a), the broad peak at 3407.04 cm^{-1} corresponded to the stretching mode of the O−H bond of the absorbed H_2O molecules in the material, and the absorption peak at 1630.39 cm^{-1} was the characteristic peak of water. In other words, the peaks at 3407.04 and 1630.39 cm^{-1} were the absorption peaks of free OH in the material in the form of physically adsorbed water under stretching vibration and

https://doi.org/10.1021/acsomega.2c07000
ACS Omega 2023, 8, 24153−24164

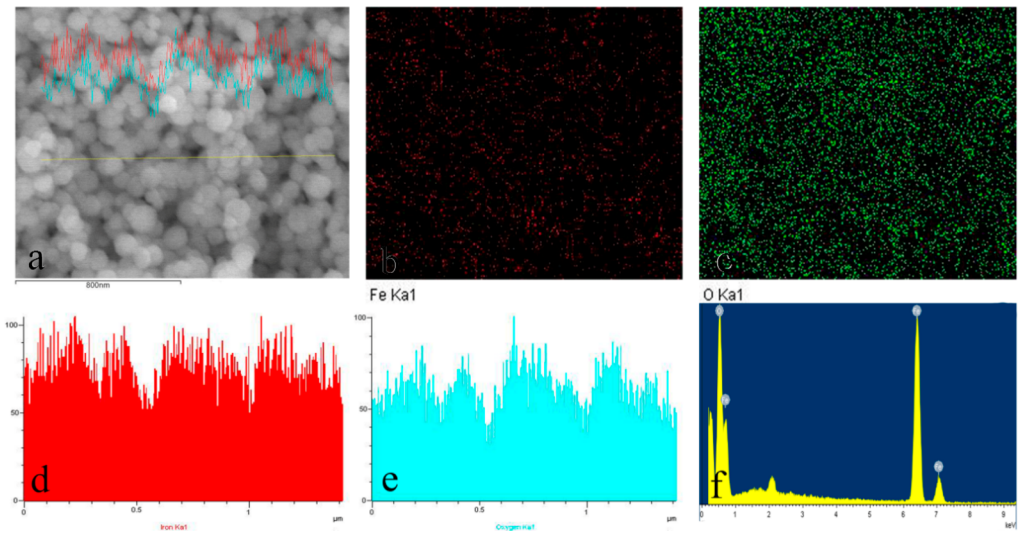

Figure 5. EDS analysis of Fe_3O_4 magnetic NPs. (a-e) The line scan and surface scan images indicated that Fe and O were widely distributed in the interior and on the surface of the magnetic NPs. (f) The resulting product was a pure iron oxide compound without other elements.

bending vibration, respectively.[17] The sharp absorption peak at 2338.25 cm^{-1} was in good agreement with the traits of CO_2 gas.[4] The absorption peak at 574.68 cm^{-1} was the characteristic peak of Fe−O in Fe_3O_4.[18] The infrared results revealed an OH modification on the surface of the Fe_3O_4. The characteristic peak near 3400 cm^{-1} was the characteristic absorption peak of multimolecular hydrogen bonds between OH and H_2O. The more evident this peak, the higher the activity of the corresponding particles, which is a characteristic manifestation of high-performance particles on IR.

Hydrodynamic Size and ζ Potential. The hydrodynamic size and ζ potential results are shown in Figure 4b (hydrodynamic size distribution and changes in zeta potential at different pH values (pH = 4, 5, 6, 7, and 8) of Fe_3O_4 magnetic NPs). When we introduced ethylene glycol, a certain number of OH modifications remained on the surface during Fe_3O_4 formation, and Fe_3O_4 hydrophilicity and stability were associated with the number of OH modifications. As shown in Figure 4b, double peaks were observed in the water phase of the Fe_3O_4 NPs, with the first peak corresponding to a particle size of approximately 355.8 ± 131.4 nm and the second peak corresponding to a particle size of approximately 2267 ± 844.9 nm. This suggests that Fe_3O_4 magnetic NPs had agglomerated in the aqueous solution. According to Figure 4b, the dispersion stability of Fe_3O_4 was weaker in an acidic environment than in an alkaline environment; that is, the NPs were prone to agglomeration in the acidic environment due to their reduced dispersion stability. Therefore, the synthesized molecular probes could undergo self-aggregation in response to the acidic tumor microenvironment.

XPS Results. Figure 4c,d shows the XPS fine spectra of Fe and O of Fe_3O_4 magnetic NPs, respectively. The peak fitting of Fe showed that the fitting peaks with binding energies of approximately 710 eV (Fe $2p_{3/2}$) and 723.5 eV (Fe $2p_{1/2}$) corresponded to Fe^{2+} [19,20] and those with binding energies of approximately 711.5 eV (Fe $2p_{3/2}$) and 725.5 eV (Fe $2p_{1/2}$) corresponded to Fe^{3+}.[21,22] The fitting peaks with binding energies of approximately 718.7 and 732.3 eV corresponded to satellite peaks.[23] An XPS quantitative analysis showed that the ratio of Fe^{2+} to Fe^{3+} on the sample surface was approximately 0.526, very close to that (0.5) in Fe_3O_4,[5] proving again that these NPs consisted of Fe_3O_4. According to peak fitting of the O 1s XPS fine spectra, the peak with binding energy ∼529.6 eV corresponded to lattice oxygen O^{2-},[24] the peak with binding energy ∼530.9 eV corresponded to surface OH^-, and the peak with binding energy ∼533.4 eV corresponded to H_2O adsorbed on the surface.

VSM Curve. The hysteresis loop detected by VSM showed that, when the magnetic field intensity changed periodically, a closed curve of hysteresis appeared in the ferromagnetic materials (Figure 4e). The VSM curve revealed that Fe_3O_4 NPs had a high M_s of approximately 75.45 emu/g. M_s can be an extremely valuable magnetic parameter for assessing the performance of permanent magnetic materials.

XRD Spectra. According to the XRD spectra of Fe_3O_4 magnetic NPs (Figure 4f), a series of characteristic diffraction peaks of Fe_3O_4 were attributed to a cubic crystal system (JCPDS 88-0315, $a = b = c = 8.375$ Å, $\alpha = \beta = \gamma = 90°$). The diffraction peaks near $2\theta = 21.3$, 35.2, 41.5, 43.4, 50.6, 63.1, 67.4, 74.3, and 78.4° corresponded to the (111), (220), (311), (222), (400), (422), (511), (440), and (531) crystal planes, respectively.[25] The diffraction peaks of the samples had a small half-height width, with a sharp shape and a small peak width, implying that they had high crystallinity. In addition, no other impurity peaks were found in the XRD spectra, suggesting that the prepared Fe_3O_4 particles had high purity.

ICP Results. The Fe in Fe_3O_4 powder was quantitatively analyzed using an ICP emission spectrometer. Different concentrations of Fe could be preconfigured for MRI to determine the effect of the Fe concentration on the magnetic resonance signal, which would provide data support for follow-up studies on CEST signal suppression. The calculation formula for the conversion of content to mg/kg is as follows: [instrument reading (13.632) × constant volume (25) × dilution factor (100)]/sampling mass (0.0496). The formula for conversion of mg/kg (mass unit) to wt % (mass percentage) is defined as follows: wt % = mg/(kg/10000), that is, 10000 mg/kg = 1 wt %. Finally, the wt % of iron is approximately 68.7117%.

EDS Spectrum Analysis. The weight and atomic percentages of Fe were 55.46% and 26.29%, respectively, and those of O were 44.54% and 73.71% (Figure 5). According to an EDS elemental analysis (Figure 5f), the resulting product was a pure iron oxide compound without other elements. The line scan and surface

https://doi.org/10.1021/acsomega.2c07000
ACS Omega 2023, 8, 24153−24164

scan (Figure 5a–e) images indicated that Fe and O were widely distributed in the interior and on the surface of the magnetic NPs, which was in line with the distribution of Fe_3O_4 NPs, further supporting the high purity of the prepared Fe_3O_4 NPs.

MRI Examination. MRI examination was used to explore the interactions between Fe_3O_4 and ioversol. The *in vitro* MRI results for Fe_3O_4 NPs (Figure 6) showed that at pH 5.0, 6.7, and 7.4 the transverse relaxation rates r_2 of magnetic resonance were 25.709 ± 2.451, 24.431 ± 2.224, and 27.375 ± 1.287 mM s^{-1}, respectively, indicating that Fe_3O_4 NPs can act as stable reference agents under different pH environments. The relaxation time T_2 was significantly shortened as the concentration of Fe_3O_4 NPs increased, signifying that Fe_3O_4 NPs can serve as magnetic resonance T_2 negative contrast agents for imaging.

The CEST effect of ioversol was determined under different field strengths and pH values. Specifically, ioversol (42 mM) solutions with different pH values (6.4, 6.6, 6.8, 7.0, 7.2, 7.4, and 7.6) were prepared and subjected to CEST scanning under the B_1 field (1.25, 2.5, 3.75, and 5.0 μT). The results showed that the CEST effect changed with the pH value, and the relationship between the CEST effect and pH was quantified by the ratio method (Figure 7). An increasingly obvious CEST effect was observed with the enhancement of the B_1 field (Figure 8). The CEST effect was completely inhibited when the Fe concentration was approximately 30 μg/mL, but when the Fe concentration was less than 10 μg/mL, both contrast agents could be imaged (Figure 9 and Table 1). The corresponding Z-spectrum is shown in Figure 10.

Inhibition Rate of Fe_3O_4. As shown in Figure 11 (inhibition rates of Fe_3O_4 under pH 7.4 and 6.5), the inhibition rates were 25.168% and 16.25% at pH 7.4 and 6.5, respectively, at a Fe_3O_4 NP concentration of 200 μg/mL, which is less than the IC_{50}. This result demonstrates that the NPs prepared in this study have no obvious cytotoxicity and thus have the potential to be used in experimental studies *in vivo*. Because of the increase in direct water saturation at the exchangeable proton frequency, the CEST effect is inhibited at high iron concentrations.

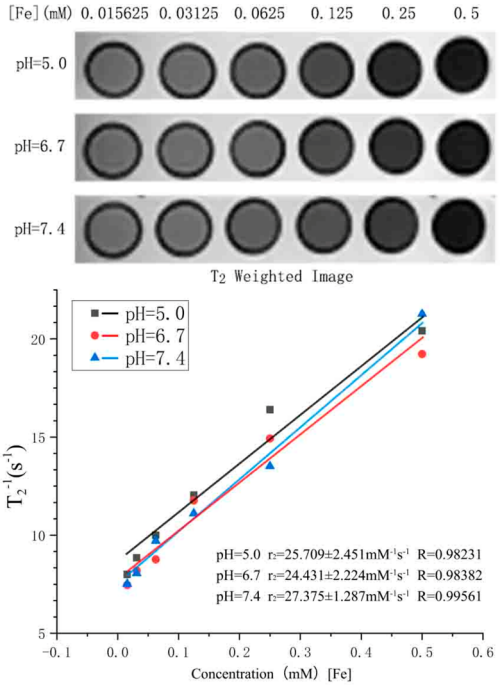

Figure 6. Changes in T_2WI and r_2 of Fe_3O_4 NPs at different concentrations and pH values.

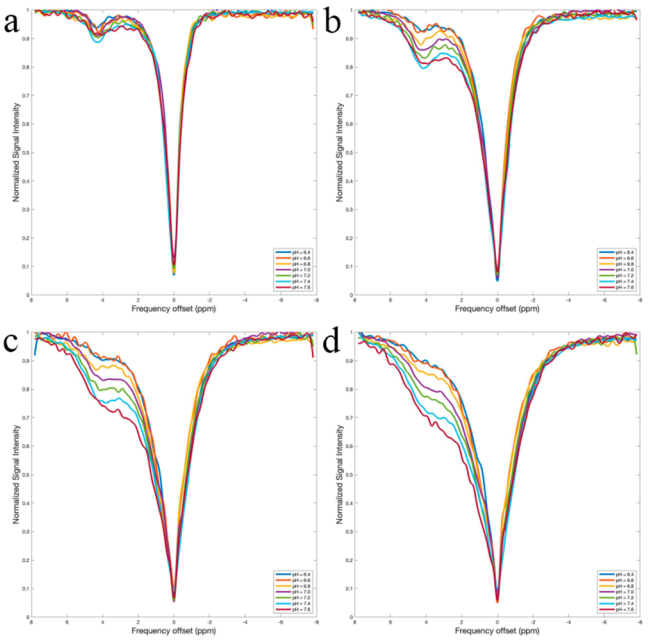

Figure 8. Correlation between the CEST effect of Ioversol and the B_1 field strength. (a–d) The B_1 fields were 1.25, 2.5, 3.75, and 5.0 μT, respectively. Ioversol (42 mM) solutions with different pH values (6.4, 6.6, 6.8, 7.0, 7.2, 7.4, and 7.6) were prepared and subjected to CEST scanning under the B_1 field.

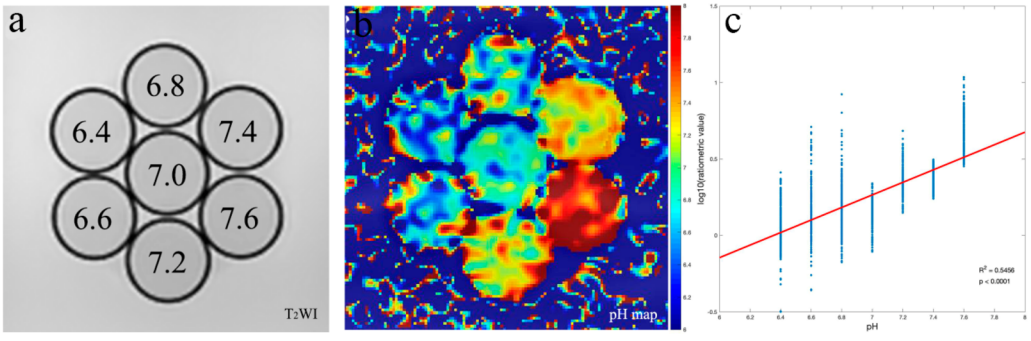

Figure 7. (a) Schematic diagram of the pH distribution of Fe_3O_4. (b) *In vitro* pH map. (c) Linear fitting between the CEST effect and pH.

https://doi.org/10.1021/acsomega.2c07000
ACS Omega 2023, 8, 24153−24164

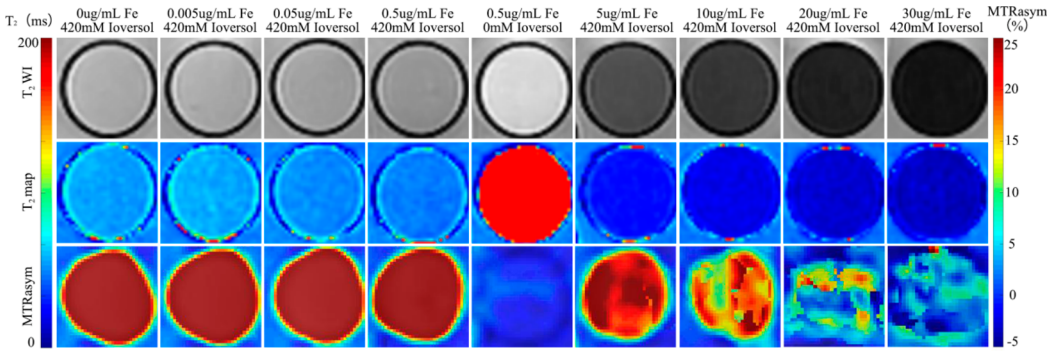

Table 1. Inhibitory Effect of Different Concentrations of Fe on Ioversol

Fe (μg/mL)	ioversol (mM)	MTR_{asym} (%)	T_1 (ms)	T_2 (ms)
0	420	35.54830417	1614 ± 68	82 ± 2
0.005	420	37.54130887	1718 ± 108	85 ± 2
0.05	420	36.21639935	1616 ± 67	78 ± 2
0.5	420	33.15679353	1467 ± 99	76 ± 2
0.5	0	0.260366789	2986 ± 125	245 ± 19
5	420	21.64297396	1480 ± 77	53 ± 1
10	420	17.79737438	1244 ± 75	46 ± 2
20	420	3.460839975	1128 ± 82	41 ± 2
30	420	−0.565267826	1036 ± 90	38 ± 2

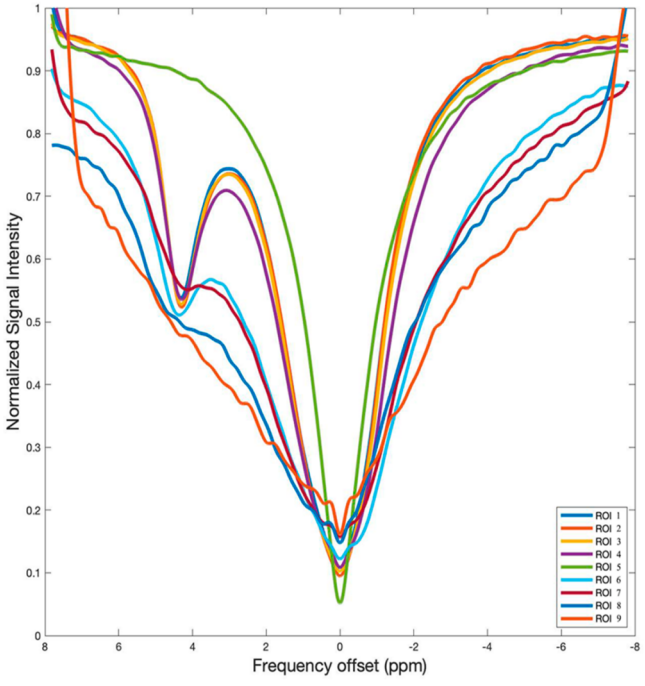

Figure 10. Z-spectrum of the inhibitory effect of different iron concentrations on the CEST effect of ioversol.

DISCUSSION

The properties (including crystallinity, size, dispersibility, morphology, and surface functional groups) of Fe_3O_4 crystals are directly affected by the Fe_3O_4 NP preparation method. Magnetic NPs with different particle sizes, morphologies, and magnetism characteristics can be prepared by changing the heating temperature, reaction time, synthesis method, and ratio

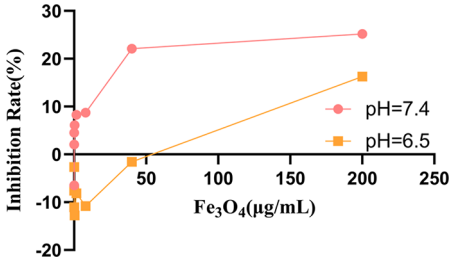

Figure 11. Results of the CCK8 experiment after Fe_3O_4 NP treatment of HCT116 cells for 24 h (pH 7.4 and pH 6.5).

of precursor to surfactant.[26] Among inorganic NPs that have been used for cancer treatment, SPIONs have been approved by the U.S. Food and Drug Administration for use in humans and applied in medical diagnosis and treatment in clinical practice,[27,28] including Feridex I.V. for liver and spleen imaging and Combidex for detecting lymph node metastasis. Iron oxide NPs are superparamagnetic; thus, SPIONs can be used as MRI contrast agents for disease diagnosis and therapeutic monitoring. In addition, the magnetic inhomogeneity of SPIONs provides a strong T_2 negative enhancement effect. Moreover, iron oxide NPs have almost negligible toxicity, and they can be absorbed and utilized by the human body after a period of cyclic degradation, since Fe is an essential trace element. However, their widespread clinical application has been hindered to some extent by the inherent properties of SPION-based T_2 contrast agents. Specifically, SPIONs decrease the signal intensity and thus lead to a negative contrast enhancement effect with reduced image brightness on T_2WI; as a result, labeled tissues may be confused with other hypointense (dark) areas, thereby interfering with the clinical diagnosis. Common dark areas include areas with calcification, bleeding in different phases, or metal deposition.[29] In addition, the high magnetic moment of SPIONs will cause local magnetic field disturbances, resulting in diffusion effects; consequently, the size of labeled tissues will be easily overestimated, and image blurriness will increase.[30−32]

In clinical practice, T_1 contrast agents are more likely to be used to enhance image brightness, thus yielding higher-resolution MR images. Targeting the aforementioned shortcomings, Kim et al.[30] developed ultrafine SPIONs (USPIONs) as T_1 contrast agents for imaging. They discovered that USPIONs with a diameter of approximately 4 nm can shorten the T_1 MRI relaxation time and complete T_1 contrast enhancement. In addition, when applying USPIONs for high-resolution blood pool T_1 imaging, various blood vessels in mouse models could be clearly displayed, including small arteries and veins and the vena cava. USPIONs can generate heat

https://doi.org/10.1021/acsomega.2c07000
ACS Omega 2023, 8, 24153−24164

under a magnetic field; therefore, they can be used in tumor thermotherapy.

In this study, magnetic NPs with an average particle size of approximately 82.6 nm were prepared and exhibited a good T_2 negative contrast enhancement effect. The ζ potential analysis revealed that Fe_3O_4 NPs had a low surface charge in an acidic environment; thus, the dispersion stability of Fe_3O_4 was weaker in an acidic environment than in an alkaline environment. That is, in an acidic environment, the NPs were prone to agglomeration due to their reduced dispersion stability. Hence, the molecular probes synthesized in this study could self-aggregate in response to the acidic tumor microenvironment. The monodispersing NaGdF4@PDA@PEG(NPP) NPs prepared by Shen et al.[33] self-aggregate at pH 5.5, 6.0, and 6.5, indicating that these NPs are also responsive to acidic microenvironments.

Generally, NPs with a surface modified with hydrophilic polymers (such as polyethylene glycol containing OH functional groups) will not be phagocytized by reticuloendothelial cells or circulating macrophages and have an increased residence time in the blood circulation, resulting in better therapeutic effects.[34] The biodistribution, pharmacokinetic characteristics, and cytotoxicity of SPIONs are mainly determined by particle size, surface modifiers, and surface charge.[35] In this study, ethylene glycol was used as the reaction solvent to provide reaction conditions for ion complexation and introducing OH functional groups. To some extent, the problem of aggregation of exposed Fe_3O_4 NPs was solved.

The size of ferrite microspheres is affected by the reaction time and the concentration of the initiator. A study[36] that explored the association between microsphere diameter and reaction time showed that at a constant temperature of 200 °C and a fixed initiator concentration (0.13 M), the diameters of ferrite microspheres were approximately 200 nm after 8 h of reaction, 400 nm at 48 h, and 800 nm at 72 h. In addition, the microsphere size is positively correlated with the initiator concentration. However, it is difficult to demonstrate a direct relationship between particle size and reaction time or change in initiator concentration, since crystals have a complex growth process. Hence, in this study, we explored how the NPs changed in size under different reaction conditions. Four reaction durations (4, 8, 12, and 16 h) were selected, and magnetic NPs of different particle sizes were prepared by changing the reaction temperature and reaction pressure. Ultimately, NPs with a particle size of approximately 82 nm were selected as the initiator for subsequent experiments.

Choi et al.[37] revealed that NPs can be completely removed from the body through urine if they have a hydrodynamic diameter of less than 5.5 nm and no contaminants on the surface. However, it is difficult to prepare particles with a diameter smaller than 5.5 nm. In addition, most NPs are large, which may result in long-term retention of inorganic nanomaterials in the body. For this reason, the biological toxicity data of NPs warrant attention. Due to their almost negligible toxicity, Fe_3O_4 NPs can be widely applied in clinical biological research. Enhanced permeability and retention (EPR) effects refer to the passive targeting process of tumor tissues, which is the major mechanism by which nanocarriers accumulate in tumor tissues. In addition, EPR effects are closely correlated with NP size. Unlike normal tissues, the vascular system of tumor tissues has a rich network of new blood vessels, impaired lymphatic drainage, and defective vascular structure. The endothelial cells are arranged neatly and tightly in normal tissues, while in tumor vessels, endothelial cells are arranged irregularly, with an irregular morphology and an expanded intercellular space (>100 mm). As a result, NPs with a size of 20−100 nm are easily retained in tumor tissues through EPR effects.[38,39] Fe_3O_4 NPs can effectively accumulate specifically in acidic tumor tissues through EPR effects, offering theoretical support for subsequent inhibition of CEST effects; that is, the CEST signal is reduced as the Fe_3O_4 concentration increases.

In this study, a 42 mM ioversol solution was prepared and then subjected to CEST scanning at different pH values (6.4−7.8) and different B_1 fields (1.25, 2.5, 3.75, and 5.0 μT). The Z-spectrum of ioversol included an obvious CEST peak at 4.3 ppm. Ioversol molecules contain two exchangeable groups, which can undergo amide proton transfer, resulting in a CEST effect. In addition, the CEST effect became more apparent with the enhancement of the B_1 field and changed with pH. Next, the relationship between the magnetization transfer rate (ST%) of ioversol and pH (6.4−7.8) was analyzed to better quantify the CEST effect. The results showed that the minimum and maximum CEST effects were observed at pH 6.4 and pH 7.8, respectively. *In vitro* experiments need to be transformed into a living-body model, and in *in vivo* research, the concentration of contrast agents injected into a living body often has a direct influence on the strength of the CEST effect. Therefore, we adopted the ratio calculation method to eliminate the effect of concentration. Since the CEST effect was different at different B_1 field strengths (1.25 and 5.0 μT), the CEST ratio was employed to quantify the changes with pH.[40]

The new imaging method combining CEST imaging and SPIONs is conducive to realizing the multidimensional quantitative analysis of tumor microenvironments. In this study, the mechanism of the coexistence of CEST and T_2 contrast agents was studied, and the concentration range of the contrast agents enabling this dual-contrast enhancement was revealed. A low Fe concentration had little impact on the CEST effect; the CEST effect declined from 35.5% to 17.8% when the Fe concentration increased from 0 to 10 μg/mL and was completely suppressed when the Fe concentration reached 30 μg/mL. It was discovered *in vitro* that, within a certain concentration range of ioversol and SPIONs, these two contrast mechanisms coexisted, and massive SPIONs might eliminate the CEST effect. SPIONs have a high specific distribution in living tissues, mainly in organs and tissues that are rich in reticuloendothelial cells, such as the spleen, liver, lymph nodes, and bone marrow. Hence, areas rich in Fe or tissues with a high concentration of SPIONs (iron deposited in brain tissues) may impede the CEST effect. Similar nonresonant saturation principles are utilized by some researchers to detect the presence of SPIO in models.[41] Based on the above findings, a nonresonant saturation pulse was applied before signal acquisition. Fe can increase the contrast by widening the water line and triggering direct saturation. The change in CEST contrast can act as a sensor of the concentration and existence of SPIONs in tissues. In one study, SPIONs and CEST contrast agents were simultaneously used to label two kinds of cells, and the cell migration status was then determined based on CEST signal changes (that is, the migration and accumulation of cells labeled with lysine-rich protein in tissues were verified by the reduction in MTR_{asym}).[42] In these studies, the migration and aggregation of cells were observed by labeling different cell populations. According to the above theory, the corresponding CEST signal will be repressed when Fe_3O_4 NPs aggregate in

https://doi.org/10.1021/acsomega.2c07000
ACS Omega 2023, 8, 24153−24164

tissue cells; thus, changes in the tumor microenvironment may be observed.

In the present study, an acid-responsive magnetic NP was prepared that could agglomerate in an acidic environment, and its size enabled it to be retained in tumor tissues through the EPR effect. When the saturation pulse was not used (that is, when the CEST effect was disabled), a T_2 negative contrast enhancement effect was observed at the sites of concentration of Fe_3O_4 NPs. Inhibition of the CEST effect was observed at the sites of concentration of Fe_3O_4 NPs when the saturation pulse was used (that is, when the CEST effect was enabled). The Fe_3O_4 NP concentration could be monitored through the reduction of the CEST effect, which indirectly reflects the changes in the microenvironment and offers new methods and dimensions for the early detection of tumors at the molecular level. In addition, a high ratio of ioversol to SPIONs was used to minimize the effect of the direct binding of iron oxide particles to ioversol. Because Fe broadens the water line, the contrast will increase as a result of direct saturation. Therefore, if used properly, the change in CEST contrast can be used as a sensor of the change in Fe concentration. When the Fe_3O_4 contrast agent migrates, the reduction of MTR_{asym} can verify the arrival and aggregation of Fe_3O_4 in the region containing the CEST contrast agent. Some tumor tissue metabolites can generate endogenous CEST signals, while cystic necrosis and fibrosis regions cannot generate the corresponding signals, which can be used to define the scope of tumor active components.

At present, our research has the following limitations. (1) The Fe_3O_4 was not further modified; thus, it cannot be applied to *in vivo* imaging. Surface modifiers need to be added to allow *in vivo* research. (2) At present, CEST imaging has been mainly used for small animal imaging under high field strength, and there has not been much research on human imaging. Further research is needed after feasibility verification to achieve clinical transformation. (3) Our research used exogenous contrast agents to generate CEST signals instead of directly using endogenous tumor substances. The complexity of human internal environment components and the presence of background CEST signal interference require the design of appropriate CEST contrast agents and optimization of the scanning sequence.

In our *in vitro* experiments, there was no interference from other exchangeable protons, and the relationship between the CEST effect and SPIONs could be investigated in isolation. There are many exchangeable protons in the body, some of which overlap with each other; thus, further exploration to eliminate background signal interference is needed prior to conducting imaging research on the living body.

CONCLUSION

The linear relationship between pH and the CEST effect was specifically described through the ratio method in this study, thus providing a theoretical basis for quantifying the change in pH of the tumor microenvironment. The CEST and SPION contrast agents can be imaged simultaneously when the SPION concentration is low, whereas high concentrations of the SPION contrast agent shut down the signal generated by the CEST contrast agent. These preliminary findings are a first step toward dual-contrast (CEST and T_2 contrast agents) imaging and are expected to be extended in *in vivo* studies in the future.

ASSOCIATED CONTENT

Data Availability Statement

The data used to support the findings of this study are included within the article.

AUTHOR INFORMATION

Corresponding Authors

Tong Tong − *Department of Radiology, Fudan University Shanghai Cancer Center, Department of Oncology, Shanghai Medical College, Fudan University, Shanghai, People's Republic of China 200032*; Email: t983352@126.com

Weijun Peng − *Department of Radiology, Fudan University Shanghai Cancer Center, Department of Oncology, Shanghai Medical College, Fudan University, Shanghai, People's Republic of China 200032*; orcid.org/0000-0002-7620-0522; Phone: +8618121299466; Email: cjr.pengweijun@vip.163.com; Fax: +862164174774

Authors

Feixiang Hu − *Department of Radiology, Fudan University Shanghai Cancer Center, Department of Oncology, Shanghai Medical College, Fudan University, Shanghai, People's Republic of China 200032*

Dan Wang − *Department of Ultrasound, Shanghai Municipal Hospital of Traditional Chinese Medicine, Shanghai University of Traditional Chinese Medicine, Shanghai, People's Republic of China 200071*

Xiaowen Ma − *Department of Radiology, Fudan University Shanghai Cancer Center, Department of Oncology, Shanghai Medical College, Fudan University, Shanghai, People's Republic of China 200032*

Tingdan Hu − *Department of Radiology, Fudan University Shanghai Cancer Center, Department of Oncology, Shanghai Medical College, Fudan University, Shanghai, People's Republic of China 200032*

Yali Yue − *Department of Radiology, Children's Hospital of Fudan University, Shanghai, People's Republic of China 200000*

Wei Tang − *Department of Radiology, Fudan University Shanghai Cancer Center, Department of Oncology, Shanghai Medical College, Fudan University, Shanghai, People's Republic of China 200032*

PuYe Wu − *GE Healthcare, Beijing, People's Republic of China 100176*

Complete contact information is available at: https://pubs.acs.org/10.1021/acsomega.2c07000

Author Contributions

F.H. and D.W. contributed equally to this work.

Author Contributions

All authors made substantial contributions to all of the following: (1) the conception and design of the study, or acquisition of data, or analysis and interpretation of data, (2) drafting the article or revising it critically for important intellectual content, (3) final approval of the version to be submitted. Publication is approved by all authors.

Funding

This work was supported by the National Natural Science Foundation of China (No. 81971687).

Notes

The authors declare the following competing financial interest(s): Puye Wu is employed by GE Healthcare, Beijing.

The remaining authors declare that the research was conducted in the absence of any commercial or financial relationships that could be construed as a potential conflict of interest.

REFERENCES

(1) Zhou, Z.; Lu, Z. R. Molecular imaging of the tumor microenvironment. *Adv. Drug Deliv Rev.* **2017**, *113*, 24−48.

(2) Shen, Z.; Chen, T.; Ma, X.; Ren, W.; Zhou, Z.; Zhu, G.; Zhang, A.; Liu, Y.; Song, J.; Li, Z.; et al. Multifunctional theranostic nanoparticles based on exceedingly small magnetic iron oxide nanoparticles for t(1)-weighted magnetic resonance imaging and chemotherapy. *ACS Nano* **2017**, *11* (11), 10992−11004.

(3) Deh, K.; Zaman, M.; Vedvyas, Y.; Liu, Z.; Gillen, K. M.; O', M. P.; Bedretdinova, D.; Nguyen, T.; Lee, R.; Spincemaille, P.; et al. Validation of mri quantitative susceptibility mapping of superparamagnetic iron oxide nanoparticles for hyperthermia applications in live subjects. *Sci. Rep* **2020**, *10* (1), 1171.

(4) Song, S.; Zhang, S.; Huang, S.; Zhang, R.; Yin, L.; Hu, Y.; Wen, T.; Zhuang, L.; Hu, B.; Wang, X. A novel multi-shelled fe3o4@mnox hollow microspheres for immobilizing u(vi) and eu(iii). *Chem. Eng. J.* **2019**, *355*, 697−709.

(5) Ghazanfari, M. R.; Kashefi, M.; Shams, S. F.; Jaafari, M. R. Perspective of fe3o4 nanoparticles role in biomedical applications. *Biochem Res. Int.* **2016**, *2016*, 7840161.

(6) Weng, Q.; Hu, X.; Zheng, J.; Xia, F.; Wang, N.; Liao, H.; Liu, Y.; Kim, D.; Liu, J.; Li, F.; et al. Toxicological risk assessments of iron oxide nanocluster- and gadolinium-based t1mri contrast agents in renal failure rats. *ACS Nano* **2019**, *13* (6), 6801−6812.

(7) Sang, M.; Luo, R.; Bai, Y.; Dou, J.; Zhang, Z.; Liu, F.; Feng, F.; Xu, J.; Liu, W. Mitochondrial membrane anchored photosensitive nano-device for lipid hydroperoxides burst and inducing ferroptosis to surmount therapy-resistant cancer. *Theranostics* **2019**, *9* (21), 6209−6223.

(8) Gobbo, O. L.; Sjaastad, K.; Radomski, M. W.; Volkov, Y.; Prina-Mello, A. Magnetic nanoparticles in cancer theranostics. *Theranostics* **2015**, *5* (11), 1249−1263.

(9) Torti, S. V.; Torti, F. M. Winning the war with iron. *Nat. Nanotechnol.* **2019**, *14* (6), 499−500.

(10) von Knebel Doeberitz, N.; Maksimovic, S.; Loi, L.; Paech, D. [chemical exchange saturation transfer (cest): magnetic resonance imaging in diagnostic oncology]. *Radiologe* **2021**, *61* (1), 43−51.

(11) Longo, D. L.; Sun, P. Z.; Consolino, L.; Michelotti, F. C.; Uggeri, F.; Aime, S. A general mri-cest ratiometric approach for ph imaging: demonstration of in vivo ph mapping with iobitridol. *J. Am. Chem. Soc.* **2014**, *136* (41), 14333−14336.

(12) Mou, J.; Liu, C.; Li, P.; Chen, Y.; Xu, H.; Wei, C.; Song, L.; Shi, J.; Chen, H. A facile synthesis of versatile cu2-xs nanoprobe for enhanced mri and infrared thermal/photoacoustic multimodal imaging. *Biomaterials* **2015**, *57*, 12−21.

(13) Gilad, A. A.; van Laarhoven, H. W.; Mcmahon, M. T.; Walczak, P.; Heerschap, A.; Neeman, M.; van Zijl, P. C.; Bulte, J. W. Feasibility of concurrent dual contrast enhancement using cest contrast agents and superparamagnetic iron oxide particles. *Magn. Reson. Med.* **2009**, *61* (4), 970−974.

(14) Ramesh, R.; Rajalakshmi, M.; Muthamizhchelvan, C.; Ponnusamy, S. Synthesis of fe3o4 nanoflowers by one pot surfactant assisted hydrothermal method and its properties. *Mater. Lett.* **2012**, *70*, 73−75.

(15) Lu, A. H.; Salabas, E. L.; Schüth, F. Magnetic nanoparticles: synthesis, protection, functionalization, and application. *Angew. Chem., Int. Ed. Engl.* **2007**, *46* (8), 1222−1244.

(16) Wu, J.; Ye, Z.; Liu, W.; Liu, Z.; Chen, J. The effect of go loading on electromagnetic wave absorption properties of fe3o4/reduced graphene oxide hybrids. *Ceram. Int.* **2017**, *43* (16), 13146−13153.

(17) Wang, H.; Sun, Y. B.; Chen, Q. W.; Yu, Y. F.; Cheng, K. Synthesis of carbon-encapsulated superparamagnetic colloidal nanoparticles with magnetic-responsive photonic crystal property. *Dalton Trans* **2010**, *39* (40), 9565−9569.

(18) Yang, S.; Zong, P.; Ren, X.; Wang, Q.; Wang, X. Rapid and highly efficient preconcentration of eu(iii) by core-shell structured fe3o4@ humic acid magnetic nanoparticles. *ACS Appl. Mater. Interfaces* **2012**, *4* (12), 6891−6900.

(19) Liu, Z.; Liu, Y.; Chen, B.; Zhu, T.; Ma, L. Novel fe−ce−ti catalyst with remarkable performance for the selective catalytic reduction of nox by nh3. *Catal. Sci. Technol.* **2016**, *6* (17), 6688−6696.

(20) Liu, C.; Xu, Q.; Tang, Y.; Wang, Z.; Ma, R.; Ma, N.; Du, P. Zr4+ doping-controlled permittivity and permeability of bafe12-xzrxo19 and the extraordinary em absorption power in the millimeter wavelength frequency range. *J. Mater. Chem. C* **2016**, *4* (40), 9532−9543.

(21) Fang, Z.; Murayama, H.; Zhao, Q.; Liu, B.; Jiang, F.; Xu, Y.; Tokunaga, M.; Liu, X. Selective mild oxidation of methane to methanol or formic acid on fe-mor catalysts. *Catal. Sci. Technol.* **2019**, *9* (24), 6946−6956.

(22) Zhou, D.; Yang, L.; Yu, L.; Kong, J.; Yao, X.; Liu, W.; Xu, Z.; Lu, X. Fe/n/c hollow nanospheres by fe(iii)-dopamine complexation-assisted one-pot doping as nonprecious-metal electrocatalysts for oxygen reduction. *Nanoscale* **2015**, *7* (4), 1501−1509.

(23) Yang, F.; Wu, C.; Yu, H.; Wang, S.; Li, T.; Yan, B.; Yin, H. The fabrication of hollow zro(2) nanoreactors encapsulating au-fe(2)o(3) dumbbell nanoparticles for co oxidation. *Nanoscale* **2021**, *13* (14), 6856−6862.

(24) Liu, X. Z.; Tang, T.; Jiang, W. J.; Zhang, Q. H.; Gu, L.; Hu, J. S. Fe-doped co(3)o(4) polycrystalline nanosheets as a binder-free bifunctional cathode for robust and efficient zinc-air batteries. *Chem. Commun. (Camb)* **2020**, *56* (40), 5374−5377.

(25) Li, B.; Rong, T.; Du, X.; Shen, Y.; Shen, Y. Preparation of fe3o4 particles with unique structures from nickel slag for enhancing microwave absorption properties. *Ceram. Int.* **2021**, *47* (13), 18848−18857.

(26) Tombácz, E.; Turcu, R.; Socoliuc, V.; Vékás, L. Magnetic iron oxide nanoparticles: recent trends in design and synthesis of magnetoresponsive nanosystems. *Biochem. Biophys. Res. Commun.* **2015**, *468* (3), 442−453.

(27) Tassa, C.; Shaw, S. Y.; Weissleder, R. Dextran-coated iron oxide nanoparticles: a versatile platform for targeted molecular imaging, molecular diagnostics, and therapy. *Acc. Chem. Res.* **2011**, *44* (10), 842−852.

(28) Arbab, A. S.; Bashaw, L. A.; Miller, B. R.; Jordan, E. K.; Lewis, B. K.; Kalish, H.; Frank, J. A. Characterization of biophysical and metabolic properties of cells labeled with superparamagnetic iron oxide nanoparticles and transfection agent for cellular mr imaging. *Radiology* **2003**, *229* (3), 838−846.

(29) Lee, N.; Hyeon, T. Designed synthesis of uniformly sized iron oxide nanoparticles for efficient magnetic resonance imaging contrast agents. *Chem. Soc. Rev.* **2012**, *41* (7), 2575−2589.

(30) Kim, B. H.; Lee, N.; Kim, H.; An, K.; Park, Y. I.; Choi, Y.; Shin, K.; Lee, Y.; Kwon, S. G.; Na, H. B.; et al. Large-scale synthesis of uniform and extremely small-sized iron oxide nanoparticles for high-resolution t1 magnetic resonance imaging contrast agents. *J. Am. Chem. Soc.* **2011**, *133* (32), 12624−12631.

(31) Gultepe, E.; Reynoso, F. J.; Jhaveri, A.; Kulkarni, P.; Nagesha, D.; Ferris, C.; Harisinghani, M.; Campbell, R. B.; Sridhar, S. Monitoring of magnetic targeting to tumor vasculature through mri and biodistribution. *Nanomedicine (Lond)* **2010**, *5* (8), 1173−1182.

(32) Arbab, A. S.; Janic, B.; Haller, J.; Pawelczyk, E.; Liu, W.; Frank, J. A. In vivo cellular imaging for translational medical research. *Curr. Med. Imaging Rev.* **2009**, *5* (1), 19−38.

(33) Shen, A.; Meng, X.; Gao, X.; Xu, X.; Shoo, C.; Tang, Z.; Liu, Y.; Bu, W.; Wang, P. An adaptable nanoplatform for integrating anatomic and functional magnetic resonance imaging under a 3.0 t magnetic field. *Adv. Funct. Mater.* **2019**, *29* (2), 1803832.

(34) Harris, J. M.; Chess, R. B. Effect of pegylation on pharmaceuticals. *Nat. Rev. Drug Discovery* **2003**, *2* (3), 214−221.

(35) Chouly, C.; Pouliquen, D.; Lucet, I.; Jeune, J. J.; Jallet, P. Development of superparamagnetic nanoparticles for mri: effect of particle size, charge and surface nature on biodistribution. *J. Microencapsul.* **1996**, *13* (3), 245−255.

https://doi.org/10.1021/acsomega.2c07000
ACS Omega 2023, 8, 24153−24164

(36) Deng, H.; Li, X.; Peng, Q.; Wang, X.; Chen, J.; Li, Y. Monodisperse magnetic single-crystal ferrite microspheres. *Angew. Chem., Int. Ed. Engl.* **2005**, *44* (18), 2782−2785.
(37) Soo Choi, H.; Liu, W.; Misra, P.; Tanaka, E.; Zimmer, J. P; Itty Ipe, B.; Bawendi, M. G; Frangioni, J. V Renal clearance of quantum dots. *Nat. Biotechnol.* **2007**, *25* (10), 1165−1170.
(38) Roberts, W. G.; Palade, G. E. Neovasculature induced by vascular endothelial growth factor is fenestrated. *Cancer Res.* **1997**, *57* (4), 765−772.
(39) Matsumura, Y.; Maeda, H. A new concept for macromolecular therapeutics in cancer chemotherapy: mechanism of tumoritropic accumulation of proteins and the antitumor agent smancs. *Cancer Res.* **1986**, *46*, 6387−6392.
(40) Goldenberg, J. M.; Pagel, M. D. Assessments of tumor metabolism with cest mri. *Nmr Biomed.* **2019**, *32* (10), e3943.
(41) Zurkiya, O.; Hu, X. Off-resonance saturation as a means of generating contrast with superparamagnetic nanoparticles. *Magn. Reson. Med.* **2006**, *56* (4), 726−732.
(42) Gilad, A. A.; Mcmahon, M. T.; Walczak, P.; Winnard, P. J.; Raman, V.; van Laarhoven, H. W.; Skoglund, C. M.; Bulte, J. W.; van Zijl, P. C. Artificial reporter gene providing mri contrast based on proton exchange. *Nat. Biotechnol.* **2007**, *25* (2), 217−219.

https://doi.org/10.1021/acsomega.2c07000
ACS Omega 2023, 8, 24153−24164